ORIGINAL RESEARCH ARTICLE

Numerical and Experimental Investigation of Residual Stress and Bond Strength in Friction Surface Cladding Process

K. Naserinejad, A. Masoumi, T.C. Bor, and M. Mosavi Mashhadi

The bond strength is an essential property of cladded products, which are produced by deposition processes such as friction surface cladding (FSC). Friction and severe plastic deformation of the deposited material cause the process to take place at elevated temperatures, and inhomogeneous cooling after the deposition process can lead to the formation of residual stresses that influence the remaining bond strength. A novel simulation method for the evaluation of the residual stress distribution in clad layer and substrate after the cladding of AA6060 onto an AA2024 substrate is proposed in this study. The effect of residual stresses on the bond strength was correlated with data gathered from 3-point bending tests aimed at the determination of the mechanical properties at the clad layer–substrate interface. The results show that on the one side, the occurrence of a higher compressive residual stress magnitude increases the bond strength, but on the other side, this relationship is not always true for average tool temperature, tool rotating speed, normal force, and tool tilt angle. Therefore, it is necessary to investigate the effect of average tool temperature, tool rotating speed, normal force, and tool tilt angle parameters on the residual stress to find the best process window for carrying out the process to have optimal bond strength.

Keywords	bond strength, friction surface cladding, residual stress

1. Introduction

In many industries, cladding of components is required to protect them against corrosion or wear. Different methods can be used for this purpose (Ref 1-3), including solid-state bonding processes. In many solid-state processes, the materials are joined together by large amounts of plastic deformation, while the process temperature is sufficiently high but low enough to avoid the melting of the materials (Ref 4). Typical examples include explosive welding (Ref 5), roll bonding (Ref 6), diffusion bonding (Ref 7), friction-stir welding (Ref 8), and friction surfacing (FS) (Ref 9). In the FS process (Ref 10), a consumable rod is rotated around its axis and forced upon a substrate plate.

K. Naserinejad, A. Masoumi, and M. Mosavi Mashhadi, School of Mechanical Engineering, College of Engineering, University of Tehran, Tehran, Iran; T.C. Bor, Chair of Production Technology, Department of Mechanics of Solids, Surfaces and Systems, Faculty of Engineering Technology, University of Twente, Enschede, The Netherlands. Contact e-mail: amasomi@ut.ac.ir.

The rotation and pressure of the consumable rod induce friction on the rod–substrate interface, causing heat generation, which enables plastic deformation at the rod–substrate interface to create solid-state bonding between the consumable rod material and the substrate. By moving the table or substrate, a continuous coating is made. However, there are a couple of drawbacks to the use of FS. Firstly, there is excessive creation of flash material that does not contribute to the deposition process. Secondly, porosity and poor bonding occur, especially on the outer edges of the coating (Ref 11). Thirdly, the thickness and width of the coating cannot be controlled easily (Ref 12).

Van der Stelt (Ref 13) introduced an improved version of FS called friction surface cladding (FSC), aiming to solve the drawbacks, which was studied in more detail by Liu et al. (Ref 14). The FSC process is illustrated in Fig. 1. It is similar to the FS process, except that there is a tool through which the consumable rod is supplied. In Fig. 1, h_0, θ, F_n, Ω, V_f, and v_t are nominal clad layer thickness, tool tilt angle, normal force, rotation velocity, constant feed rate, and translation speed, respectively.

Taking the FSC setup as a starting point, Liu (Ref 15), using AA1050 and AA2024-T351 as the coating and substrate, has investigated which process parameters can be used to create a smooth and defect-free clad layer. She reported that the substrate temperature should be above 317 °C; otherwise, no continuous layers were deposited. The mixing of clad material and substrate material occurred when the substrate temperature became higher than 407 °C. Hence, the tool rotation speed should be selected with care along with the layer thickness and layer width to ensure the process takes place within the temperature range defined by these bounds.
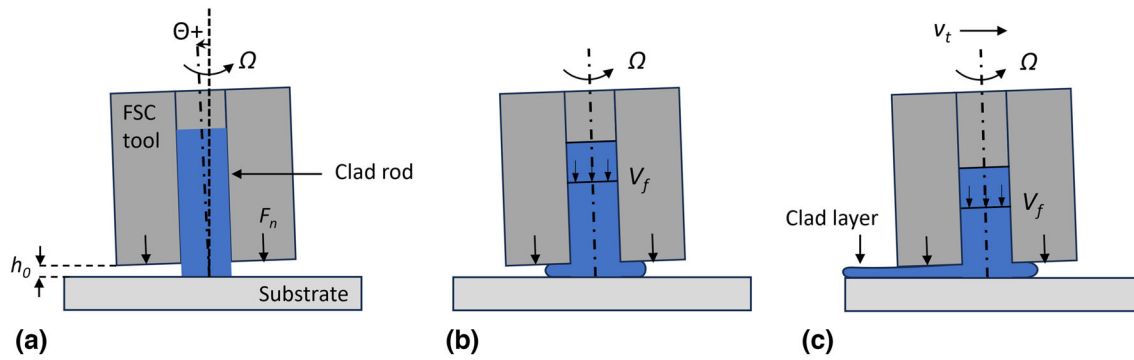
Fig. 1 Schematic overview of the FSC process (Ref 14), θ: tool tilt angle, Ω: tool rotation velocity (rpm), F_n: normal tool force, h_0: predefined height from the substrate, V_f: consumable rod constant feed rate, v_t: tool/substrate translation speed
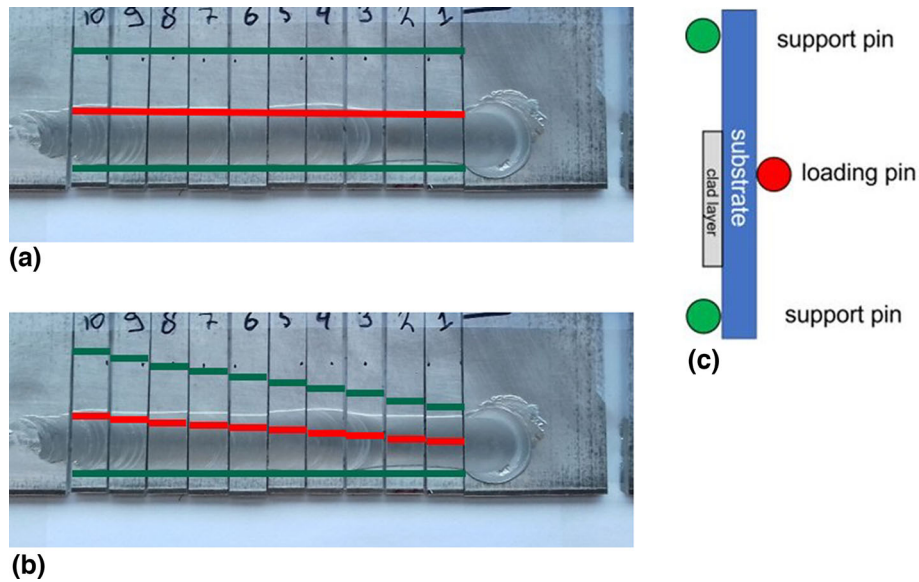

Fig. 2 Three-point bending samples extracted from AA2024-T351 substrate deposited with AA6060-T6 clad layer with the FSC process. Green and red indicate the position of the support pins and the loading pin of the three-point bending test performed, respectively. (a) Loading pin located near the lateral edge of the clad layer, series A. (b) Loading pin located at various locations from the lateral edge toward the middle of the clad layer, series B. (c) Experimental configuration (Ref 16) (Color figure online)

The coating–substrate bond strength is a critical aspect of the FSC process. Liu et al. (Ref 14) reported that no debonding occurred in a short 3-point bending test for the evaluation of the bond strength. Koning (Ref 16) studied the bond strength using similar 3-point bending tests after the deposition of a thin layer of AA6060 on top of an AA2024 substrate employing the same FCS process. He studied the effects of the process temperature and the tool tilt angle. Process temperatures were selected from approximately 280 to 350 °C as measured within the substrate, and the tool tilt angle was varied between − 1 to 3 degrees. Two series of 3-point bending tests were performed for which details are shown in Fig. 2. In the first series (A), the loading pin was located near the lateral edge location. In the second series (B), the loading pin location was varied from the lateral edge toward the center of the deposited layer. A good assessment of the bonding of the clad layer to the substrate could be made based on the first and the second series results.

A typical example of a sample after the 3-point bending test is shown in Fig. 3. In this sample, the support pins were placed symmetrically with respect to the loading pin. The loading pin

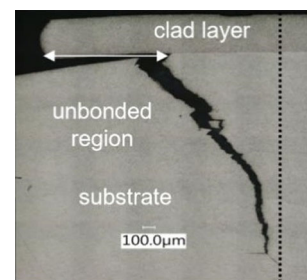**Fig. 3** Example of a sample after a 3-point bending test (process temperature 300 °C) (Ref 16)

was located at the bottom of the substrate at the end of the dotted line. During the 3-point bending test, the clad layer came loose from the substrate, as indicated by the "unbonded region".

Possibly some crack growth occurred subsequently along the clad layer–substrate interface. At the final stages of the test,

a crack developed from the interface toward the middle of the substrate. It suggests that the interface of the clad layer and the substrate was able to withstand crack growth along the interface during the bending test leading to the development of a crack from the interface into the substrate. Analyses of all 3-point bending tests indicated that the least lateral edge debonding occurred at the highest temperatures (350 °C) and with a tool tilt angle of 0 degrees.

On the other hand, the residual stress affects the bonding strength. Residual stresses are dependent on the process parameters and the participating materials of coating and substrate. Idema (Ref 17) has studied the residual stress states at the surface of the deposited coating after the deposition of AA1050 onto an AA2024 substrate through FSC employing X-ray diffraction (XRD). Residual stress measurements showed a compressive biaxial stress state for all clad layer specimens. The compressive stress state determined was attributed to elastic recovery at the end of the deposition process when the FSC tool was released from the surface. The compressive forces exerted on the substrate through the clad layer disappeared, and the elastic expansion in the vertical direction was accompanied by a small in-plane compression due to the Poisson effect explaining the residual stress state in the clad layer.

Recently, the residual stress distribution in an FSC-similar process (additive friction-stir deposition) was reported (Ref 18). The reported residual stresses ranged between − 127 and 91 MPa. Another FSC-similar process is friction-stir welding (FSW). The residual stress is the concentration point of several FSW investigations (Ref 19). The effect of residual stress on the bond strength was investigated for the cold-spray process (Ref 20), where it was found that the bonding strength is highly affected by the residual stress. However, no such studies exist for the FSC-similar processes.

Based on the reviewed literature, it can be concluded that the bond strength is in general influenced by the materials of coating and substrate, the process parameters, and the residual stresses generated during the FSC process. The role of the residual stresses requires further investigation. Therefore, in the present study, the FSC process is modeled using ABAQUS software and the residual stress distribution obtained is reported and discussed. The numerical modeling method is validated by experimental data from hole-drilling residual stress measurements. Subsequently, the correlation between the residual stress state and the coating–substrate bond strength is also investigated employing the produced data from the simulation analysis.

2. Numerical Model

2.1 Model Description

The thermomechanical model of the FSC process was developed assuming steady-state conditions. The FSC tool translates with respect to the substrate surface and deposits the clad layer. It is assumed that after some distance covered, the process conditions remain constant for the remainder of the deposition process. Hence, the process can be simulated through an Eulerian approach with a stationary control volume where substrate material and clad material will flow through. The modeling method is similar to that of Schmidt and Hattel
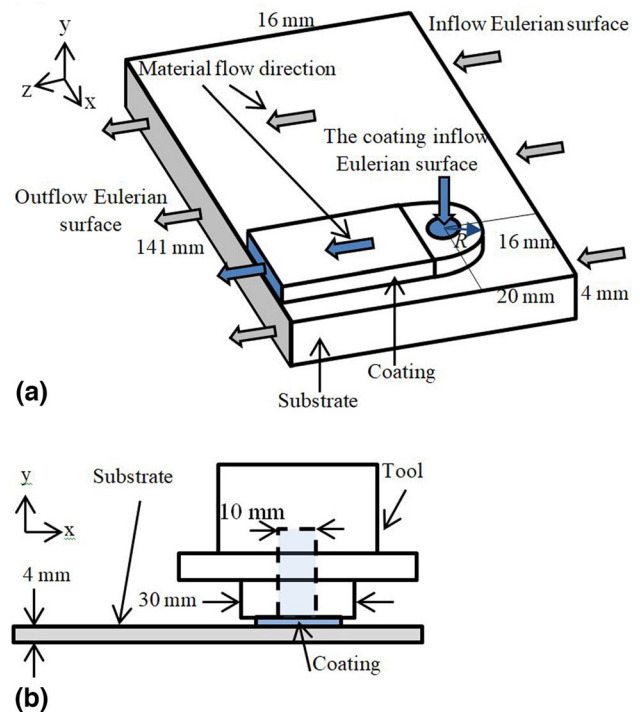

Fig. 4 (a): Schematic of the FSC thermomechanical model pertaining to the stationary phase of friction surface cladding of a thin clad layer on top of a substrate. The tool was left out for clarity. Substrate material flows through the control volume from right to left (see gray arrows). Clad material enters through the blue boundary near the tool (see also blue arrow) and flows with the same velocity as the substrate to the end of the control volume on the left; (b): The assembly side view; the thin coating is located between the tool and the substrate

(Ref 21), who worked extensively on the simulation of the FSW process. Their model comprised a disk-shaped workpiece with a hole in the center, providing space for the FSW tool pin. They prescribed a material inflow surface along the leading half of the disk circumference and a material outflow along the other half of the disk. Similar methods have been used by other researchers (Ref 22-26) to model the thermomechanical processes during FS.

In this work, the inflow and outflow surfaces were defined for both the substrate and the coating to simulate the FSC process, as shown schematically in Fig. 4(A). The modeling method in the present study is close to the actual FS and FSC processes in two aspects. First, there are no disks for modeling the coating and substrate, as there are not any in the actual process. A half-disk and an attached rectangular prism are assumed for the coating and a rectangular cube for the substrate, as shown in Fig. 4(A). Second, there is only one inlet flow for the coating, and there is only one outlet flow from the coating.

It should be declared that the model configuration is the same as "configuration 2" in (Ref 14). The same configuration is used in 3-point bending FSC samples as detailed in Fig. 2. In this figure, the dashed region can be assumed to be the simulation region during the deposition phase. In Fig. 4(A), the inflow Eulerian surface on the coating has a 10-mm-diameter circle boundary, which is the same as the hole diameter in the FSC tool. The diameter of the half circle (2R) is equal to the coating width. The rigid rotating tool is located on the coating

top surface (Fig. 4(B)) and exerts a process-induced normal force F_n.

2.2 Governing Equations and Boundary Conditions

2.2.1 Thermal. To calculate the temperature distribution in the coating and substrate, a similar approach to the friction-stir welding (FSW) process (Ref 27) is pursued. The governing equation is based on 3D heat conduction with dedicated boundary conditions defined within an orthogonal *xyz* coordinate system. The time- and place-dependent temperature distribution, $T(x,y,z,t)$, is calculated using the heat diffusion equation (Ref 28):

$$\frac{\partial}{\partial x}\left(k\frac{\partial T}{\partial x}\right) + \frac{\partial}{\partial y}\left(k\frac{\partial T}{\partial y}\right) + \frac{\partial}{\partial z}\left(k\frac{\partial T}{\partial z}\right) + \dot{q} = \rho c_p \frac{\partial T}{\partial t} \tag{Eq 1}$$

where k is the heat conductivity, $\dot{q}$ is the thermal energy generation rate, ρ is the density, c_p is the specific heat at constant pressure, and t is time. Convective heat loss is defined on outer surfaces (Eulerian surfaces are excluded) through (Ref 29):

$$k\frac{\partial T}{\partial n} = -h_f(T - T_S) \tag{Eq 2}$$

where h_f and T_S are the heat transfer coefficient and the ambient temperature, respectively. Another boundary condition of Eq 1 is the temperature distribution at $t = 0$ ($T(x,y,z,0)$). The last boundary condition comprises the frictional heat at contact surfaces (for example, the FSC tool and the coating contact surfaces) due to relative motion, following (Ref 24):

$$k\frac{\partial T}{\partial n} = \mu \cdot p \cdot \dot{\gamma} \tag{Eq 3}$$

where μ is the friction coefficient, p denotes the pressure, and $\dot{\gamma}$ is the sliding rate at the contact surface. Frictional heat may also be calculated by (Ref 30):

$$k\frac{\partial T}{\partial n} = \int \omega \cdot dM = \int \omega \cdot r \cdot \tau \cdot dA \tag{Eq 4}$$

where ω is the tool angular rotation speed ($\omega = 2\pi\Omega/60$), M is the torque supplied to the cladding tool, τ is the shear stress, and A is the contact area where frictional heating occurs. The contribution due to plastic deformation in Eq 1 is given by Ref 29:

$$\dot{q}_{\text{plastic deformation}} = \eta \cdot S\dot{\varepsilon}^{pl} \tag{Eq 5}$$

where η is the ratio of the plastic work to thermal energy transformation, S is the deviatoric stress, and $\dot{\varepsilon}^{pl}$ is the plastic strain rate.

For finite element (FE) calculations, typically, the rate form of Eq 1 is employed (Ref 24):

$$C(t)\dot{T} + K(t)T = Q(t) \tag{Eq 6}$$

where C is the capacitance matrix, T represents the temperature vector, K is the conductivity matrix, and Q is the heat vector. Here, C, T, and K are time-dependent, and $\dot{T}$ denotes the time derivative of the temperature. In fast load varying problems, it is suggested to use explicit direct integration (Ref 31). In the explicit approach used in our model, $\dot{T}$ is calculated using Ref 32:

$$\dot{T}_{(i)}^N = \left(C^{NJ}\right)^{-1}\left(P_{(i)}^J - F_{(i)}^J\right) \tag{Eq 7}$$

where T^N is the temperature at node N and the subscript i refers to the increment number in an explicit dynamic step, C^{NJ} is the lumped capacitance matrix, P^J is the vector of applied nodal source, and F^J is the vector of internal flux. Using the explicit forward-difference time integration rule, which is used in the coupled thermal-stress analysis, the current temperature is calculated by:

$$T_{(i+1)}^N = T_{(i)}^N + \Delta t_{(i+1)}\dot{T}_{(i)}^N \tag{Eq 8}$$

2.2.2 Mechanical. For the mechanical response, the principle of linear momentum must be satisfied for any continuum in motion, whether a solid or a fluid. That is (Ref 33):

$$\text{div } P + \rho B = \rho\,\ddot{u} \tag{Eq 9}$$

where P is the stress tensor, B is the body force vector, and $\ddot{u}$ is the acceleration vector. The matrix form of Eq 9 would be (Ref 24):

$$m\ddot{u} + I = F \tag{Eq 10}$$

where m, F, and I are the mass matrix, external force vector, and internal force vector, respectively. The mechanical solution response in a fully coupled thermal-stress analysis is obtained using the explicit central-difference integration rule with a lumped mass matrix. Therefore, similar to what was illustrated for the current temperature in Eq (8), the current displacement or rotation would be $u_{(i+1)}^N$ from equation (10) through (Ref 32):

$$\ddot{u}_{(i)}^N = \left(m^{NJ}\right)^{-1}\left(F_{(i)}^J - I_{(i)}^J\right) \tag{Eq 11}$$

$$u_{(i+1)}^N = u_{(i)}^N + \Delta t_{(i+1)}\dot{u}_{\left(i+\frac{1}{2}\right)}^N \tag{Eq 12}$$

where Δt represents the time increment.

2.3 Residual Stress Modeling

2.3.1 Modeling Approach. To investigate the residual stress, 4 FSC experiments were numerically modeled using ABAQUS software. The experiments are named experiments number 1 to 4. The numerical models of these experiments are numbered in the same way. Tool temperature, tool rotating speed, normal force, and tool tilt angle have different values in these experiments. However, it is tried to keep the tool temperature at a certain value manually. Therefore, these experiments can be distinguished by the average tool temper-

Table 1 The average tool temperature in different experiments and corresponding process parameters (Ref 16)

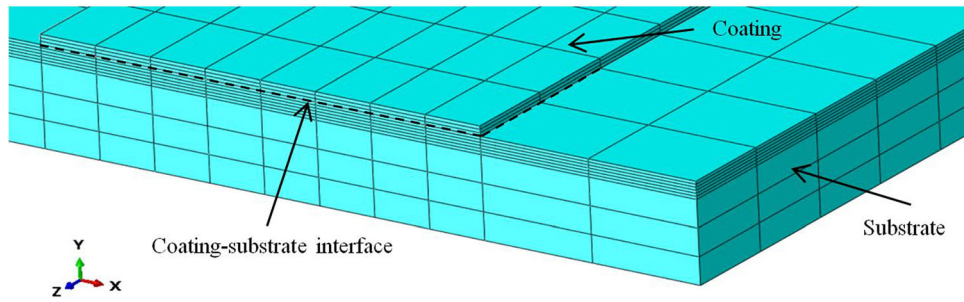| Experiment number	1	2	3	4
Average tool temperature, °C	330	316	330	286
Average tool rotating speed Ω, rpm	410	340	450	330
Normal force F_n, kN	5.8	8.05	5.8	7.24
Tool tilt angle $\theta°$	1	0	0	0
Average coating thickness, mm	0.24	0.34	0.37	0.37

Fig. 5 The mesh in coating and substrate with smaller elements close to the coating–substrate interface

Table 2 Coating dimensions and the total number of elements of the coating and substrate in different models

		Coating width, mm	Coating thickness, mm	Total number of coating elements	Total number of substrate elements
Model number	0	16.7	0.35	678	4707
	1	20.4	0.24	642	4284
	2	17.2	0.34	642	4446
	3	16.4	0.37	642	4446
	4	16.22	0.37	642	4446

Table 3 Thermal and elastic properties of the materials

	AA1050	AA6060	AA2024-T351	H13 steel
Density, kg/m^3	2705 [34]	2705	2770 [34]	7760 [35]
Poisson ratio	0.33 [36]	0.33	0.33 [34]	(The tool is assumed to be rigid)
Thermal expansion coefficient, μm/m K	25.5 [34]	23 [16]	24.7 [34] (for AA2024)	13.1 [35]

ature, as shown in Table 1. The exploratory FSC setup was not equipped with advanced temperature control. Instead the tool temperature was adjusted manually. While performing the experiments, the operator checked the temperature as indicated by the thermocouple placed in the bottom of the FSC tool head, close to the central opening from where the clad material was deposited onto the substrate. As soon as the measured temperature started to deviate from the desired value, the operator either slightly increased or decreased the tool rotation rate, depending on the observed temperature development. In this way, it was possible to keep temperature changes to a minimum. The tool rotation speed in Table 1 is an average of tool rotation speed during the FSC process. The variation of the tool rotating speed either creates more deformation and friction to increase the process temperature, or less deformation and friction to decrease the process temperature. It should be noted that the tool temperature is the temperature of the "point t". See section 4-1.

The coating material in experiments 1 to 4 was AA6060, and the substrate material was AA2024-T351. Before numerically modeling these experiments, another experiment was numerically modeled using AA1050 material for the coating. This model was named "model number 0". This single numerical model aimed to validate the modeling method. The tool material in all experiments is H13 steel. The coating thickness varied in different experiments.

2.3.2 Implementation in ABAQUS. ABAQUS is widely used for finite element analysis. Here, we use the ALE approach of this solver. In our model, there are 3 and 9 C3D8RT elements through the thickness of the coating and substrate, respectively. As discussed later, the experimental method used for residual stress measurement reports through-thickness residual stresses up to 1 mm depth. Therefore in the substrate, the elements that are located near the coating have smaller heights than other elements that are located further away from the interface with the coating (Fig. 5). The total number of elements in the coating and substrate is shown in Table 2. The tool is meshed using 352 C3D8T elements.

It should be noted that an initial temperature distribution is imposed on all parts in the FEM model to achieve the steady state in a shorter time. The initial temperature distribution is relatively close to the temperature distribution expected based on previous experimental and simulation work. The relevant thermal and elastic material properties of the materials are given in Tables 3, 4, and 5, respectively.

The tool is considered a rigid body, and the substrate is an elastic part that does not deform plastically during the deposition of the coating material. It should be mentioned that in the experiments numbers 1 to 4, no coating/substrate mixing occurred, see Fig. 6. A temperature-dependent elastic perfect-plastic model is employed to describe the AA1050 coating plastic properties pertaining to model number 0. The elastic modulus of AA1050 and its plastic deformation behavior is obtained from literature data (Ref 15).

Figure 7(A) shows the plastic properties of AA1050. It is worth noting that, at strain rates above approximately 10 (s^{-1}), the flow stress is almost constant, independent of the strain rate (Ref 15). Hence, it is assumed that the strain rate was always

Table 4 Thermal conductivity and specific heat capacity used for the materials [15, 16, 34, 35, 37, 38]

	Temperature, °C	Conductivity, W/m·K	Temperature, °C	Specific heat capacity, J/kg·K
AA2024-T351	20	164	21	879
	104	182	101	932
	203	194	203	988
	302	203	302	1059
	402	210	402	1124
	502	217	451	1153
	554	220	…	…
AA1050	…	231	…	900
AA6060	…	190	…	900
	…			
H13 Steel		28.4	…	600

Table 5 Modulus of elasticity for the materials [16, 34-36]

	H13 Steel			AA1050	AA6060	AA2024
Temperature, °C	20	260	540	…	…	…
Modulus of elasticity, GPa	210	185	150	70	68	72.4

Fig. 6 Microscopic image of FSC experiment number 4. Clearly, no macroscopic mixing of coating and substrate occurred at the interface.

higher than 10 (s^{-1}), and strain-rate dependency of plastic properties was disregarded.

For model numbers 1 to 4, the strain-rate dependence of the plastic behavior of AA6060 was incorporated through the use of literature data. The data are displayed below in Fig. 7(B) to Fig. 7(D). It should be mentioned that the ABAQUS software uses linear interpolation and extrapolation (Ref 32).

The penalty friction formulation is used for the tool/coating contact. The temperature-dependent friction coefficients for this contact are given in Table 6. It is assumed that 100% of the frictional work is converted into heat (Ref 25) and the heat is equally distributed over the surfaces which are in contact. On the other hand, because in our ALE steady-state numerical modeling, the coating and substrate regions act like a control volume, it is assumed that the coating material sticks completely to the substrate.

In other words, the coating contact surface has the same velocity as the substrate contact surface. As a result of this assumption, the sliding frictional heat generation between the coating and the substrate is neglected, while as can be seen in Fig. 1, this source of heat plays an essential role in the FSC process, at least during startup phases A and B. To overcome this problem, a portion of sliding frictional heat is defined on the two adjacent surfaces as a heat flux boundary condition. To calculate the frictional heat using Equation (4), the friction coefficient should be known. The minimum friction coefficient for AA1050/AA2034-T351 contact is given by μ_0, which is a function of temperature (Ref 41) (Table 7). According to the typically experienced process temperatures (Table 1), μ_0 is assumed to be 1 when the process is in a stationary state during FSC. It should be

noted that the heat transfer between the adjacent surfaces is controlled by a heat transfer coefficient equal to 8500 W/m²K (Ref 42). This portion of frictional heat is neglected in model numbers 1 to 4, where AA6060 is deposited on top of AA2024 as the compression force increased significantly in these experiments. In other words, it is assumed that due to this high magnitude of compression force, the coating sticks directly to the substrate, and no relative motion occurred during the deposition when the process is the stationary phase (see Fig. 4(A) caption).

The other heat generation source is plastic deformation. It is assumed that 90% of the plastic dissipation rate appears as a heat flux per unit volume (Ref 26, 32). For this heat generation and transfer, convection heat transfer is defined on the tool and substrate surfaces, excluding the Eulerian ones (see also Fig. 4(A)). The convection coefficient (h) varies from 10 to 400 W/m²K depending on each surface situation (10 W/m²K for free surfaces, 200 W/m²K for tool/tool holder contact, and 250 to 400 W/m²K for different regions of the substrate).

3. Experimental Work

3.1 Residual Stress Measurement

The incremental hole-drilling test was used to determine residual stresses in the coating and the substrate. The test was implemented using the directions of the ASTM-E837-13a standard. Figure 8(A) and (B) shows the test setup and the strain gauge on the FSC test sample, respectively. The hole is
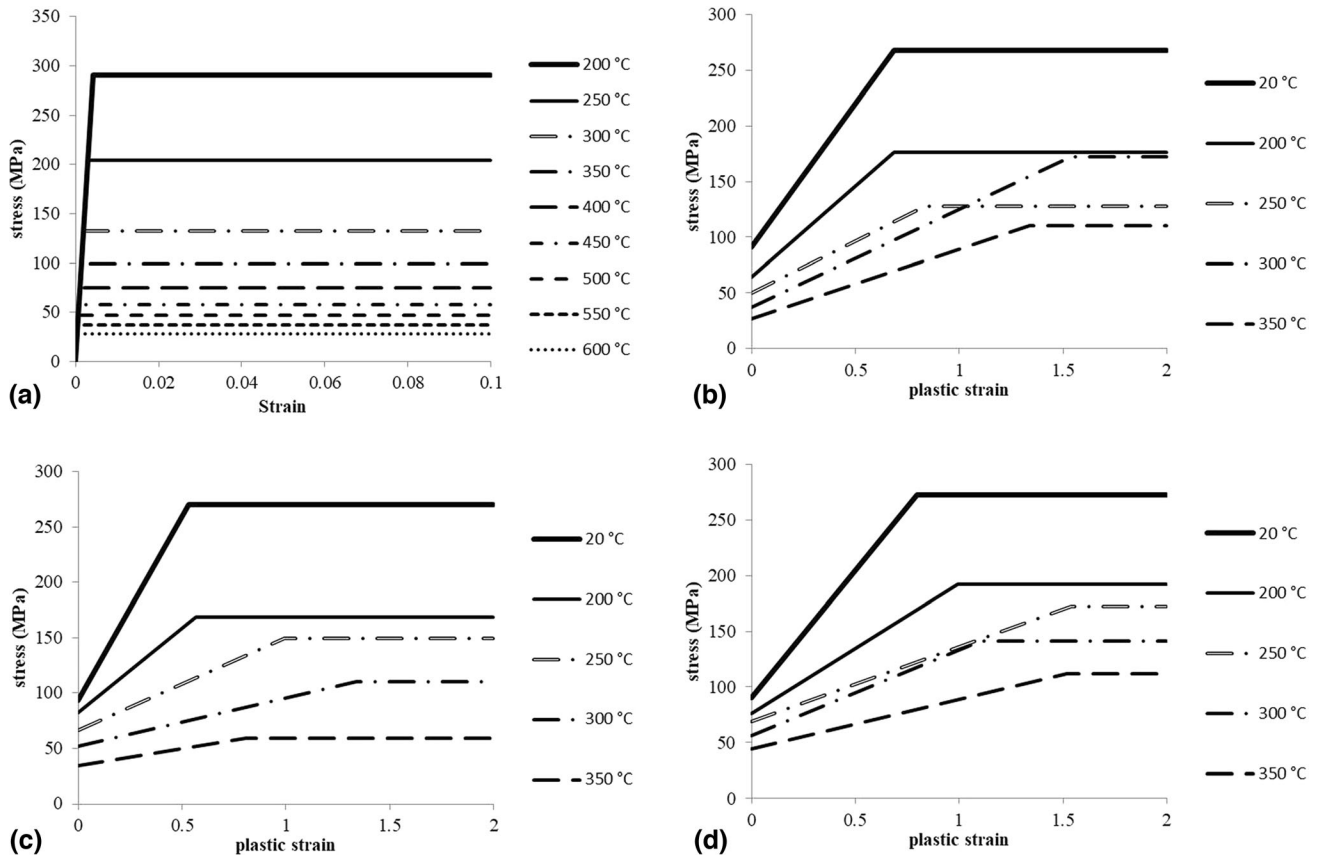
Fig. 7 (a): The plastic behavior of AA1050, elastic-perfect plastic properties assumption using data from [15]. (b), (c) and (d): The plastic behavior of AA6060, strain rate = 0.01, 1, and 350, respectively; elastic-linear-perfect plastic properties assumption using data from [39]

Table 6 Temperature-dependent friction coefficients for tool/coating contact [40]

Temperature, °C	0	34.7	93.3	147.5	210.6	260	315.6	371.1	426.7
Friction coefficient	0.61	0.545	0.359	0.255	0.244	0.147	0.135	0.02	0.007

Table 7 The minimum friction coefficient for AA1050/ AA2024-T351 contact [41] required for modeling the heat generation during modeling the deposition of AA1050 on top of AA2024 (model 0)

| Temperature, °C	150	200	250	300	350
Friction coefficient, $\mu 0$	0.3	0.5	0.6	1	1

drilled in the center of the strain gage. This test can determine through-thickness stress values up to 1 mm depth with 0.025 mm steps. At each step of drilling, the stresses are calculated using data from the strain gauge. The reported residual stresses are in the form of longitudinal, transverse, and shear stresses.

The FCS samples were produced from the experimental work of Liu (Ref 15) and Idema (Ref 17). To validate the numerical modeling method presented in this paper, the

experimental process parameters of the tested FSC sample are used in the numerical model with number 0.

3.2 Bond Strength Measurement

3.2.1 Test Method. The 3-point bending test method was used to obtain information about the bond strength between the AA6060 coating and the AA2024 substrate (experiment numbers 1 to 4). The setup of the 3-point bending test can be split up into two parts: the machine and the samples. The tests were performed on the Zwick/Roell Z5.0 mechanical test machine, using a standard test program according to the ASTM D 2344 standard. The machine setup was not changed during the testing except for the support width. The samples varied a bit in size but were aimed to be quite similar. From the 3-point bending tests, force and deflection data were gathered. The samples from the FSC experiments were cut using a band saw and a circular disk saw. An example of the cutting results can be seen in Fig. 2. The width of the samples was aimed to be 10 millimeters, and the lengths of the sample were at least 40 millimeters. The samples were oriented such that the coating
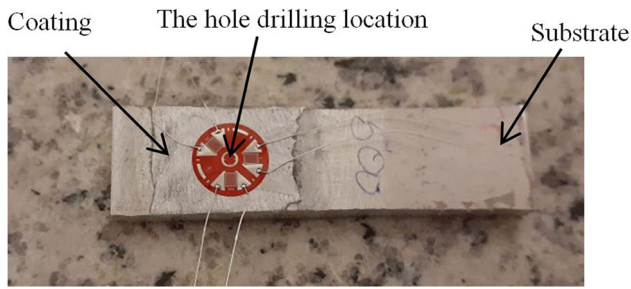
(a)

(b)

Fig. 8 (a):The incremental hole-drilling test setup used for residual stress measurement, and (b): The FSC test sample with installed strain gage (in red)

was facing downward and the support rods of the 3-point bending setup were placed outside of the coating region. The force was exerted to the substrate opposite of the coating by the downward motion of the middle support of the test machine (Fig. 9).

3.2.2 Bond Strength Definition. An explorative 3-point bending test was conducted on an FSC sample. The sample deflection at the failure point was about 4 mm. It was seen by the naked eye that the outer region of the clad layer has debonded and thereafter a crack occurred under the debonded area. Hereafter, the sample of the explorative test was put under a light microscope to take a closer look. The crack was initiated at exactly the end of the debonded part of the clad layer. The crack then grew into the substrate material until the 3-point bending test was terminated. Because of this location, the crack seemed to have been instigated by a stress concentration due to the debonding of the outer clad layer.

In the 3-point bending test, the coating plays a reinforcement role for the substrate. The failure of the sample seems to be the result of debonding of the coating, and the maximum stress in the sample was defined as a measure of bond strength. This stress was determined as follows. The 3-point bending tests were conducted on the samples of experiments number 1 to 4. The sample deflection was set equal to the distance traveled by the middle support. Force–deflection curves were prepared from the gathered data of the 3-point bending test. Then, from the force–deflection curves, stresses and strains were computed.

The strain was calculated using the curvature of the sample during the 3-point bending test. The stress was calculated using adapted Euler–Bernoulli equations, which accounted for large deformation, coating on the substrate, and large deflections (Ref
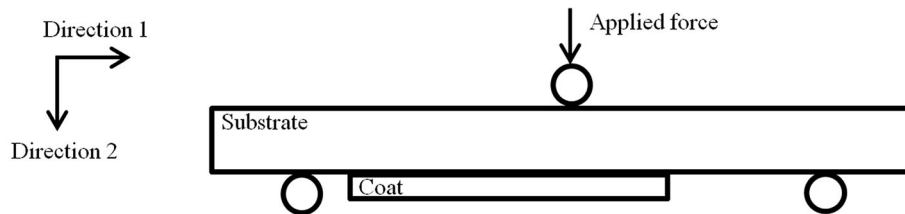

Fig. 9 Three-point bending test Schematic view. Direction 1 is along the substrate–coating interface and direction 2 is normal to the interface.
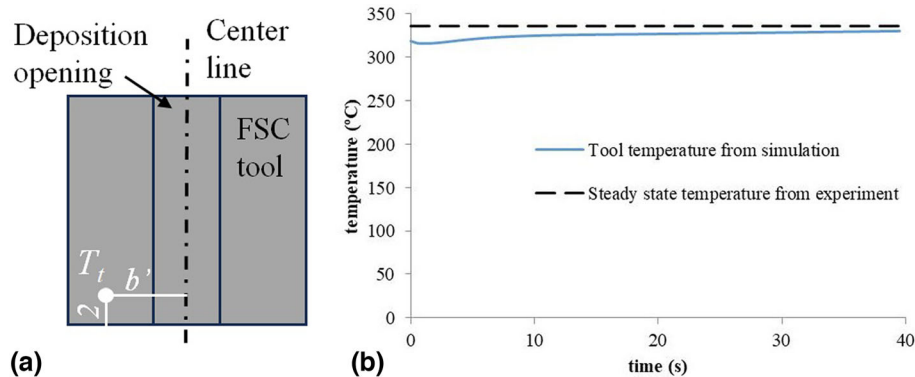

(a)

(b)

Fig. 10 (a): The position of the wireless thermocouple in the tool (dimension in mm) [15], and (b): The temperature history of a node on the tool in the FEM modeling of experiment number 0 (solid line), used for steady-state criterion. Average tool temperature from experiment 0 given by dashed line
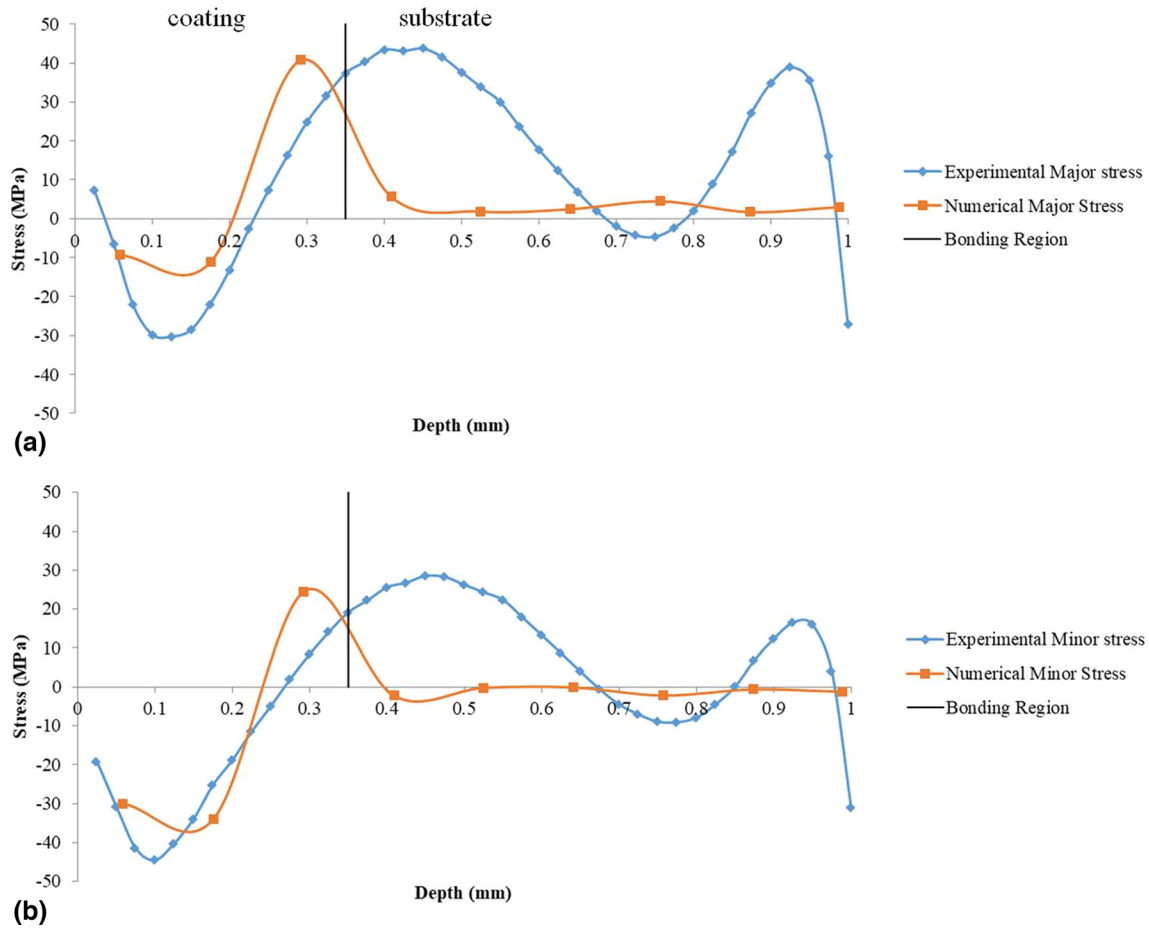
Fig. 11 Model validation comparing experimental and numerical minor stress in FSC sample depth for an AA1050 layer deposited on AA2024 (experiment and simulation number 0); (a): Major stress, and (b): Minor stress

43, 44). The average of maximum values of this adapted stress in the samples is taken from these graphs for comparison.

4. Results and Discussion

4.1 Residual Stress Results

The numerical modeling in the present study aimed to achieve an evaluation of important process-related parameters in the steady state of the FSC process. During the experimental process, the tool temperature was measured using a wireless thermocouple. This thermocouple measured the temperature at a certain point on the tool named "point t". The position of this point is shown by T_t in (A). In this figure b' is 8 mm. In the numerical model, a node named "node t" was selected on the tool. The "node t" had the same location as "point t" did. Comparison of the temperature history of "point t" and "node t" was used for steady-state achievement evaluation in the numerical model. For experiment number 0, the reported temperature for "point t" was approximately 336 °C for about 50 seconds in the steady-state portion of the temperature history (Ref 15). The steady-state achievement in the numerical modeling can be confirmed from "node t" temperature history in Fig. 10(A). By comparing the point t temperature history and Fig. 10(B), it can be concluded that the tool steady-state

temperature is almost achieved in the numerical model. Note that the initial temperature of "node t" has a value near the "point t" as a well estimated temperature distribution was used as a starting point to reduce the time to reach a steady-state condition as mentioned in section 2.3.2. It is worth noting that achieving the steady-state temperature in such a complex process with large number of process parameters and with the contribution of high-speed plastic deformation and also friction and bonding modeling difficulties can be assumed as an essential part of numerical modeling validation.

The same tool temperature-based comparison was used for experiments 1 to 4. The coating process modeling was continued until the steady-state condition was almost reached. After the heating part of the modeling, the next part started, which was the cooling process. There is no tool and normal force in the cooling process. The cooling process continued until a near-room temperature was achieved for the coating and substrate. After the cooling process, the residual stresses can be obtained from the model.

4.2 Validation

As discussed in the previous subsection, a part of validation was done by comparing the tool steady-state temperature in the numerical model and the experimental FSC process. The residual stresses were extracted from the model after the cooling process. As mentioned before, the result of the residual
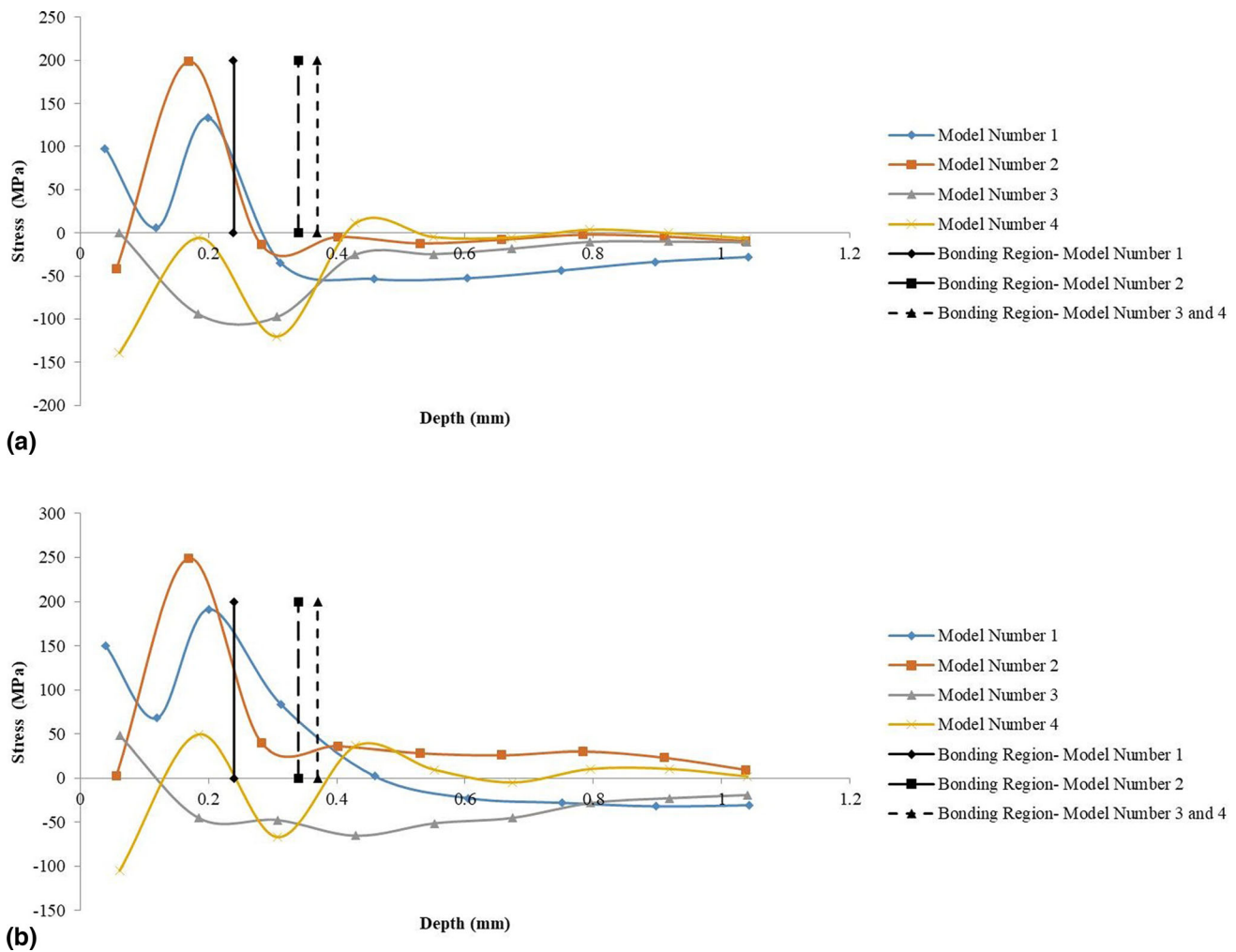
Fig. 12 Through-thickness residual stress in directions (a): 1 and (b): 2, along the coating and substrate depth in models 1 to 4. Direction 1 is along the substrate–coating interface and direction 2 is normal to the interface. The locations of the coating–substrate interfaces are indicated by the respective vertical lines.

Table 8 The relation between different residual stress measures in the coating and the bond strength

Model number	1	2	3	4
Minimum residual stress in the coating in direction 1, MPa	6	− 42	− 97	− 139
coating stress values close to the bonding region in direction 1, MPa	133	− 13	− 97	− 120
Minimum residual stress in the coating in direction 2, MPa	67	3	− 47	− 105
coating stress values close to the bonding region in direction 2, MPa	191	40	− 47	− 66
Bond strength, MPa	402	412	424	437

stress hole-drilling test was used for validation of the numerical modeling method. Major (maximum) and minor (minimum) stresses at each depth were calculated using Mohr's circle equations. These calculations were done both for the experimental test and numerical (model number 0) results. Therefore, these results are independent of the stress orientation and can be compared with each other.

As can be seen in Fig. 11 (A) and (B), there is an acceptable agreement between experimental and numerical results. The marker points show the value of calculated (numerical model) or measured (experimental test) stress. Most of the calculated residual stress values are located near the

measured residual stress curve. Especially in the coating region (from depth 0 mm to the "bonding region"), there is a better agreement between the experimental values and curves derived from the numerical model. The two curves have an intersection near the bonding region. This means that the numerical model was almost successful in calculating the residual stress in the coating and its bonding region with the substrate.

It should be noted that there is no step in the residual stress curves at the coating–substrate interface. Similar thermal expansion of the coating and substrate (Table 3) can be a major reason for this curve continuity. On the other hand, the long time between experiment number 0 and the hole-drilling
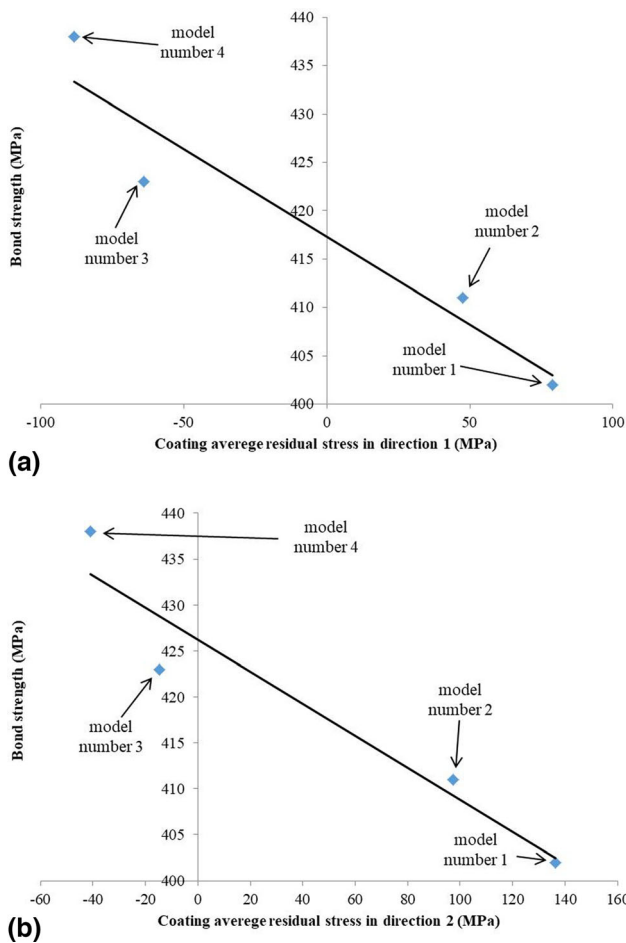
Fig. 13 Relationship between average coating residual stress in directions (a): 1, (b): 2; and bond strength of FSC sample in 3-point bending test. Direction 1 is along the substrate–coating interface and direction 2 is normal to the interface.

test dates may be another reason for some stress relief and resulting curve smoothing.

The observed deviation between modeling and experimental results in Fig. 11 may have some reasons. First, the cutting of the FSC sample before experimental residual stress measurement can have a changing effect on the residual stress. Second, there is a significant time duration (almost six years) between the FSC experiment and residual stress measurement. Third, the hole-drilling method may have some errors. Fourth, the steady-state assumption in the modeling and limited geometrical model size, which were intended to limit the computational cost of the problem, affects the results.

A result of these limitations is that the convective or radiation heat transfer cannot be defined on the Eulerian surfaces, while the heat transfer is present in the same regions in the actual FSC experiment.

4.3 Residual Stress Effect on Bond Strength

Having determined both (i) residual stresses of model numbers 1 to 4 by a validated method and (ii) bond strength values of the FSC samples from 3-point bending tests, the relation between residual stress and the bond strength can be investigated. The residual stresses in direction 1 of the coating and substrate close to the bonding line were selected as the

residual stress measure. The direction 1 is shown in Fig. 9 and runs parallel to the substrate–coating interface. The stress in direction 1 in the coating during the 3-point bending test would be in general positive (tension) based on the imposed deformation in Fig. 9 configuration. Therefore, a negative residual stress can act inversely and delay the separation of the coating and the substrate. On the other hand, positive stress in direction 2 tends to separate the coating from the substrate. This means that negative residual stress in direction 2 can delay the coating-substrate separation, too.

As can be seen in Fig. 12(A) and Table 8, the coating residual stress values in direction 1, close to the bonding region, clearly decrease from model number 1 to model number 4. A similar relationship exists between average coating thickness residual stresses (Fig. 13(A)) and minimum residual stress in the coating (Fig. 12 and Table 8). Average coating thickness residual stresses mean the average of stress values in the elements located through the thickness. The same trends can be seen in the residual stresses in direction 2 (Fig. 12(B), Fig. 13(B)).

It can be concluded from Fig. 12, 13 and Table 8 that the lower residual stresses in directions 1 and 2 result in higher bond strengths between the coating and the substrate. This is in agreement with the expected relationship between the residual stress and the bond strength as suggested above. In Table 1, which shows process parameters, comparing the tool average temperature and maximum stress in the 3-point bending test shows that the above relationship is not always true for average tool temperature. In other words, the tool average temperature cannot be a proper indicator of the bond strength.

5. Conclusions

The FSC process is a newly developed solid-state cladding process in which the bond strength is an essential property of cladded products. The severe plastic deformation and the high temperatures in the FCS process result in residual stresses being developed in the coating and substrate. The present study aimed to propose a novel simulation method for the evaluation of the residual stress distribution in the coating and the substrate after the cladding process of an AA6060 coating on an AA2024 substrate. The proposed simulation method was validated using residual stress data obtained from the experimental hole-drilling method. As the bond strength is affected by the residual stress, the effect of residual stress on bond strength was correlated with data gathered from the 3-point bending test. The outcomes of this research are as follows:

- The lower residual stress results in a higher bond strength
- This fact is valid for the lowest coating stress values, average coating stress values, and the coating stress values close to the bonding region; in directions 1 and 2
- This relationship is not always true for average tool temperature, tool rotating speed, vertical pressuring force, and tool tilt angle.
- Therefore, it is necessary to investigate the effect of average tool temperature, tool rotating speed, vertical pressuring force, and tool tilt angle parameters on the residual stress to find the best windows for carrying out the process to have the best possible bond strength.

References

1. M. Awang, A.A. Khalili, and S.R. Pedapati, A Review: Thin Protective Coating for Wear Protection in High-Temperature Application, *Metals*, 2020, **10**, p 42.

2. R. Ranjan and A.K. Das, Enhancement of Mechanical and Corrosion Protection Properties of Different Substrates after Friction Surfacing: A Concise Review, *Mater. Today: Proc.*, 2022, **57**, p 2111–2115.

3. R. Ranjan and A. Kumar Das, Protection from Corrosion and Wear by Different Weld Cladding Techniques: A Review, *Mater. Today: Proc.*, 2022, **57**, p 1687–1693.

4. R.F. Tylecote, SOLID PHASE WELDING OF METALS: St. Martin's Press, 1968

5. P. Manikandan, K. Hokamoto, A.A. Deribas, K. Raghukandan, and R. Tomoshige, Explosive Welding of Titanium/Stainless Steel by Controlling Energetic Conditions, *Mater. Trans.*, 2006, **47**, p 2049–2055.

6. V. Jindal, V. Srivastava, and R. Ghosh, Development of IF Steel–Al Multilayer Composite by Repetitive Roll Bonding and Annealing Process, *Mater. Sci. Technol.*, 2008, **24**, p 798–802.

7. R. Jiangwei, L. Yajiang, and F. Tao, Microstructure Characteristics in the Interface Zone of Ti/Al Diffusion Bonding, *Mater. Lett.*, 2002, **56**, p 647–652.

8. K. Wang, H.A. Khan, Z. Li, S. Lyu, and J. Li, Micro Friction Stir Welding of Multilayer Aluminum Alloy Sheets, *J. Mater. Process. Technol.*, 2018, **260**, p 137–145.

9. K. Badheka and V.J. Badheka, Friction Surfacing of Aluminium on Steel: An Experimental Approach, *Mater. Today: Proc.*, 2017, **4**, p 9937–9941.

10. J. Dilip, S. Babu, S.V. Rajan, K. Rafi, G.J. Ram, and B. Stucker, Use of Friction Surfacing for Additive Manufacturing, *Mater. Manuf. Process.*, 2013, **28**, p 189–194.

11. J. Gandra, R. Miranda, and P. Vilaça, Performance Analysis of Friction Surfacing, *J. Mater. Process. Technol.*, 2012, **212**, p 1676–1686.

12. J. Gandra, H. Krohn, R.M. Miranda, P. Vilaça, L. Quintino, and J.F. dos Santos, Friction Surfacing—A Review, *J. Mater. Process. Technol.*, 2014, **214**, p 1062–1093.

13. A.V.D. Stelt, (2014) Friction Surface Cladding; Development of a Solid State Cladding Process, Ph.D. Thesis, University of Twente, Enschede, The Netherlands

14. S. Liu, T.C. Bor, A.A. Van der Stelt, H.J.M. Geijselaers, C. Kwakernaak, A.M. Kooijman et al., Friction Surface Cladding: An Exploratory Study of a New Solid State Cladding Process, *J. Mater. Process. Technol.*, 2016, **229**, p 769–784.

15. S. Liu, (2016) Friction Surface Cladding of AA1050 onto AA2024; Parameter Study and Process Window Development, Ph.D. Thesis, University of Twente

16. R. Koning, (2018) Analysis of the Bond Strength of Clad Layers Deposited through Friction Surface Cladding, Master of Science Thesis, University of Twente

17. D. Idema, (2020) Texture and residual stress characterization of Aluminum Clad Layers Deposited through Friction Surface Cladding, Master Thesis, Faculty of Engineering Technology, Mechanics of Solids Surfaces and System Production Technology, University of Twente, 2020

18. N. Zhu, D.Z. Avery, Y. Chen, K. An, J.B. Jordon, P.G. Allison, et al., (2022) Residual Stress Distributions in AA6061 Material Produced by Additive Friction Stir Deposition, *Journal of Materials Engineering and Performance*,

19. J.H. Hattel, M.R. Sonne, and C.C. Tutum, Modelling Residual Stresses in Friction Stir Welding of Al alloys—A Review of Possibilities and Future Trends, *Int. J. Adv. Manufact. Technol.*, 2015, **76**, p 1793–1805.

20. R. Singh, S. Schruefer, S. Wilson, J. Gibmeier, and R. Vassen, Influence of Coating Thickness on Residual Stress and Adhesion-Strength of Cold-Sprayed Inconel 718 Coatings, *Surf. Coat. Technol.*, 2018, **350**, p 64–73.

21. H. Schmidt and J. Hattel, A Local Model for the Thermomechanical Conditions in Friction Stir Welding", *Model. Sim. Mater. Sci. Eng.*, 2004, **13**, p 77–93.

22. S.M. Bararpour, H. Jamshidi Aval, and R. Jamaati, Modeling and Experimental Investigation on Friction Surfacing of Aluminum Alloys, *J. Alloys Compound*, 2019, **805**, p 57–68.

23. Z. Rahmati, H. Jamshidi Aval, S. Nourouzi, and R. Jamaati, Modeling and Experimental Study of Friction Surfacing of AA2024 Alloy Over AA1050 Plates, *Mater. Res. Exp.*, 2019, **6**, p 0865g2.

24. S.M. Bararpour, H. Jamshidi Aval, and R. Jamaati, An Experimental and Theoretical Investigation of Thermo-Mechanical Issues in Friction Surfacing of Al-Mg Aluminum Alloys: Material Flow and Residual Stress, *Model. Sim. Mater. Sci. Eng.*, 2020, **28**(3), p 035003.

25. P. Pirhayati and H. Jamshidi Aval, Phase-field Microstructure Simulation during Aluminum Alloy Friction Surfacing, *Surf. Coat. Technol.*, 2020, **402**, p 126496.

26. S.M. Bararpour, H. Jamshidi Aval, and R. Jamaati, Cellular Automaton Modeling of Dynamic Recrystallization in Al-Mg Alloy Coating Fabricated using the Friction Surfacing Process, *Surf. Coat. Technol.*, 2021, **407**, p 126784.

27. K.N. Salloomi, F.I. Hussein, and S.N.M. Al-Sumaidae, Temperature and Stress Evaluation during Three Different Phases of Friction Stir Welding of AA 7075–T651 Alloy, *Model. Sim. Eng.*, 2020, **2020**, p 3197813–3197898.

28. F.P. Incropera, D.P. Dewitt, T.L. Bergman, and A.S. Lavine, (2007) *Fundamentals of Heat and Mass Transfer*, Sixth edition.: John Wiley & Sons

29. R. Hamilton, D. MacKenzie, and H. Li, Multi-physics Simulation of Friction Stir Welding Process, *Eng. Comput.*, 2010, **27**, p 967–985.

30. M.B. Djurdjanovic, M.M. Mijajlovic, D.S. Milcic, and D.S. Stamenkovic, Heat Generation During Friction Stir Welding Process, *Tribol Indust.*, 2009, **31**(8), p 14.

31. R.D. Cook, D.S. Malkus, M.E. Plesha, and R.J. Witt, (2001) *CONCEPTS AND APPLICATIONS OF FINITE ELEMENT ANALYSIS* FOURTH EDITION ed.: JOHN WILEY & SONS

32. "SIMULIA User Assistance (Abaqus Documentation)," ed

33. W.M. Lai, D. Rubin, and E. Krempl, *Introduction to Continuum Mechanics*, Forth edition ed.: Elsevier, 2010

34. *ASM Handbook Formerly Tenth Edition, Metals Handbook* vol. Volume 2: ASM International, 1990

35. *ASM Handbook Formerly Tenth Edition, Metals Handbook* vol. Volume 1: ASM International, 1990

36. S.M. Alavizadeh, K. Abrinia, and A. Parvizi, Twisted Multi Channel Angular Pressing (TMCAP) as a Novel Severe Plastic Deformation Method, *Metals Mater. Int.*, 2020, **26**, p 260–271.

37. W. Li, Z. Zhang, J. Li, and Y.J. Chao, Numerical Analysis of Joint Temperature Evolution During Friction Stir Welding Based on Sticking Contact, *J. Mater. Eng. Perform.*, 2012, **21**(9), p 1849–1856.

38. M. Shabgard, S. Seydi, and M. Seyedzavvar, Novel Approach Towards Finite Element Analysis of Residual Stresses in Electrical Discharge Machining Process, *Int. J. Adv. Manufact. Technol.*, 2016, **82**, p 1805–1814.

39. V. Vilamosa, A.H. Clausen, T. Børvik, S.R. Skjervold, and O.S. Hopperstad, Behaviour of Al-Mg-Si alloys at a Wide Range of Temperatures and Strain Rates, *Int. J. Impact Eng*, 2015, **86**, p 223–239.

40. R. Česnavičius, S. Kilikevičius, P. Krasauskas, R. Dundulis, and H. Olišauskas, Research of the Friction Stir Welding Process of Aluminium Alloys, *MECHANIKA*, 2016, **22**, p 291–296.

41. H. Geijselaers, A. van der Stelt, and T. Bor, Dry friction during sliding of AA1050 on AA2024 at elevated temperature, *Proc. Eng.*, 2017, **207**, p 1671–1676.

42. A.A. Fashami, M.H. Hoda, N.B. Gollo, M. Arab, and B. Nami, The Numerical Modeling to Study the Multi-Pass Friction Stir Processing on Magnesium Casting Alloy AZ91, *ADMT J.*, 2019, **12**(4), p 9–16.

43. H. Deng, H. Shi, and S. Tsuruoka, Influence of Coating Thickness and Temperature on Mechanical Properties of Steel Deposited with Co-based Alloy Hardfacing Coating, *Surf. Coat. Technol.*, 2010, **204**, p 3927–3934.

44. J.M. Gere and S.P. Timoshenko, *Mechanics of Materials*, second edition ed.: Thornes Ltd